

Testing Automated Solar Flare Forecasting With 13 Years of MDI Synoptic Magnetograms

J.P. Mason¹, J.T. Hoeksema¹

JMason86@sun.stanford.edu, JTHoeksema@sun.stanford.edu

ABSTRACT

Flare occurrence is statistically associated with changes in several characteristics of the line-of-sight magnetic field in solar active regions (AR). We calculated magnetic measures throughout the disk passage of 1,075 ARs spanning solar cycle 23 in an attempt to find a statistical relationship between the solar magnetic field and solar flares. This expansive study of over 71,000 magnetograms and more than 6,000 solar flares uses superposed epoch analysis to investigate changes in several magnetic measures surrounding all X-class, M-class, B- and C-class flares, as well as ARs completely lacking associated flares. The results were used to seek out any pre- or post- flare signatures with the advantage of the capability to recover weak systematic signals with superposed epoch (SPE) analysis. SPE analysis is a method of combining large sets of data series in a manner that yields concise information. This is achieved by aligning the temporal location of a specified flare in each time series, then calculating the statistical moments of the "overlapping" data. The best calculated parameter, the gradient-weighted inversion-line length (GWILL), combines the primary inversion line (PIL) length and the gradient across it. Therefore, GWILL is sensitive to complex field structures via the length of the PIL and shearing via the gradient. GWILL shows an average 35% increase during the 40 hours prior to X-class flares, a 16% increase before M-class flares, and 17% increase prior to B-C-class flares. ARs not associated with flares tend to decrease in GWILL during their disk passage. Gilbert and Heidke skill scores are also calculated and show that even GWILL is not a reliable parameter for predicting solar flares in real time.

Subject headings: Sun: activity; Sun: solar flares; Sun: magnetic fields; Methods: statistical; skill score

¹W. W. Hansen Experimental Physics Laboratory, Stanford University, 450 Serra Mall, Stanford, CA 94305-4085

1. Introduction

Awareness of space weather and its implications for sensitive technologies has been steadily increasing. As society becomes more technologically dependent on complex global systems, the potential risk posed by the geomagnetic response to solar variability increases. Adverse effects include large-scale power distribution failure, Global Positioning Satellite tracking errors, high-frequency radio communication interference, and low-orbit satellite drag (NRC 2008). These issues originate in the interaction between the interplanetary magnetic field in the solar wind and the Earth’s magnetosphere, as well as powerful radiation from solar flares. The spawning point for these phenomena is almost always solar active regions (ARs).

Schrijver (2008) described a process of solar flare initiation based on previously published models. When field lines snap to a lower energy configuration via reconnection, the excess energy released produces coronal mass ejections (CMEs) and/or solar flares (e.g. Silva et al. 1996; Metcalf et al. 1995). Nonpotential energy is stored in the magnetic fields (e.g. Tanaka and Nakagawa 1973; Krall et al. 1982), the parameterization of which is an active area of research (e.g. Falconer et al. 2002, 2003, 2008; Leka and Barnes 2003a, 2003b; Barnes and Leka 2006; Song et al. 2006). Schrijver (2008) also calls for more statistically significant studies based on consistent and long-duration observations of ARs, such as the present analysis.

This investigation explores the magnetic field parameterizations proposed in previous studies. To date, there are no consistent, long-duration vector-field observations available. Thus the parameterizations we chose to study were restricted to quantities derivable from longitudinal magnetograms. In addition, we wanted parameters robust enough to be calculated with little or no user interaction in order to (1) facilitate the application to a large data sample, and (2) remove user-generated bias. After obtaining preliminary results, parameters that lacked an indication for further analysis were no longer pursued (see section 2.2.4). The most promising parameters that satisfied the above criteria were the total unsigned flux, bipolar region separation, and the gradient-weighted inversion-line length.

These parameters confirm the findings of other investigations over many years. Guo and Zhang (2006) tested a possible measure of nonpotentiality deemed the *effective distance*, the distance between the flux-weighted centers of the bipolar region constituting the AR, and found that it correlates well with flaring intensity. Falconer et al. (2001) tested the correlation between AR CME productivity and several possible measures of nonpotentiality, such as the length of the strong-shear, strong-field primary inversion line. Falconer et al. (2003) generalized the measure for line-of-sight magnetograms. Schrijver (2007) defined a similar measure called R that parameterized the unsigned flux near high-gradient, strong-

field polarity-separation lines. Leka and Barnes (2003b) showed that the predictive capability of any of these measures based on longitudinal magnetograms is not particularly strong, even when multiple measures are combined to optimize their predictive ability.

Most previous studies have either been restricted to a relatively small sample size or neglected the time evolution of the magnetic field. Leka and Barnes (2007) showed that removing these two limitations is critical to improving the ability to understand and predict solar flares. This study expands the earlier work to a time-sensitive and statistically significant sample using the 13-year record of Michelson Doppler Imager (MDI) synoptic line-of-sight magnetograms.

2. Data and Method

2.1. Initial Data Collection and Extraction

This study uses the recalibrated level 1.8, 96-minute cadence line-of-sight full-disk magnetograms from the MDI instrument (Scherrer et al. 1995) onboard the Solar and Heliospheric Observatory (SOHO). These products are available from 1996 to the present with relatively few gaps. The present investigation analyzes the 1,075 ARs visible in the record that span most of the interval from April 15, 1996 to December 31, 2008.

Very few selection criteria were applied to this initial dataset. All of the numbered National Oceanic and Atmospheric Administration (NOAA) ARs within this time period were considered. ARs needed to be observed in at least three magnetograms within 30 degrees of disk center to be included. This reduces the influence of projection effects that distort the MDI measurements far from disk center. Erroneous and incomplete images were removed.

The “FindAR” program described here uses the SolarSoftWare IDL library (Freeland and Handy 1998) and is available online¹. The only required user input for FindAR are NOAA AR numbers, which can be input individually or by range. FindAR can also accept a date range and compile the relevant NOAA AR numbers automatically. The program accesses the online NOAA daily solar regions database, which provides the location, type and approximate size for each region. The catalog information is used to identify and extract a rectangular sub-image from each of the full-disk MDI magnetograms that includes the AR. A buffer area was added around each rectangular AR to ensure that all elements of

¹<http://soi.stanford.edu/data/tables>

the AR are included. The buffer size scales with the size of the AR and is adjusted to maintain a constant re-mapped image size for a given AR during the disk passage. The MDI group’s *project* module was used to extract sub-images and remap the image using a Postel equidistant azimuthal projection. This map projection yields consistent estimates of distance on the solar surface, which was necessary for the reliable calculation of the magnetic measures. Figure 1 shows an example of a series of sub-images as the AR crosses the disk. Calculations were performed on the remapped images to characterize the evolving AR parameters. These calculations were performed using our ”Solignis” program, which includes the code for FindAR and requires no additional user input. Solignis generates all the necessary data to perform a statistical analysis of all the parameters included in the code. This code can be found at the same URL as FindAR and can be used as the framework for other researchers to perform similar long-duration, consistent database studies with the caveat that they must have access to the MDI full-disk magnetograms.

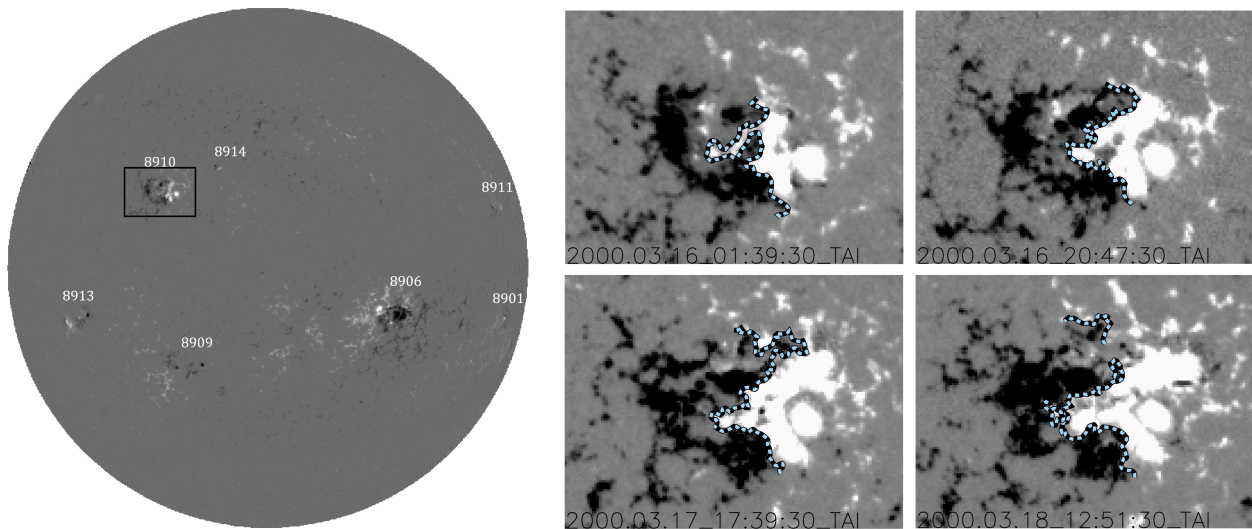


Fig. 1.— The evolution of NOAA AR 8910 as it passes within 30 of disk center. A full-disk magnetogram is shown on the left and four projected images from March 16-18, 2000 are shown on the right. Central meridian passage for this AR occurred on March 18. The dashed line indicates the calculated primary inversion line (PIL).

2.2. Calculated Parameters

This section details the four parameters chosen as proxy measurements of the non-potentiality and/or magnetic complexity of the ARs. The selection of parameters was based on their predictive success in previous studies.

2.2.1. *Total Unsigned Magnetic Flux*

The unsigned total magnetic flux is a straightforward sum of the absolute value of the longitudinal magnetic field measurements. As mentioned in Section 2.1, large ARs have a large buffer area. This effect causes a modest skew in the flux estimate that slightly amplifies the total for regions that are already larger (Bokenkamp 2007). However, the field values in the buffer region are typically weak and contribute little to the total flux. Measurements of the strong magnetic field in the umbrae of sunspots (>3 kG) are saturated in the MDI data (Liu et al. 2007) and this tends to bias the total flux value downward. These competing effects are nontrivial to correct, and may slightly influence the value of this variable. We apply a minimum threshold of 100G in our calculation to reduce the effect of noise and to reduce the contribution of the quiet sun outside the ARs.

Total flux is a commonly used parameter (e.g. Falconer et al. 2002, Leka and Barnes 2003b) that provides a rough measure of the size and strength of an AR. Leka and Barnes (2003b) found that contrary to the conventional wisdom, total flux alone is not a good predictor of flares. We chose to include this parameter to provide additional weight for contradicting the conventional wisdom.

2.2.2. *Primary Inversion Line Length*

Polarity inversion lines separate patches of positive and negative flux. These occur all over the sun and are effectively continuous within ARs (see dashed lines in Figs. 1 and 2). The primary polarity inversion line (PIL) separates the major polarity regions of an AR. This line is relatively easy to trace by eye but presents a challenge for computer software to quantify. Bokenkamp (2007) developed an IDL program based on a routine written by Falconer et al. (2003) to effectively define the PIL using a 3-iteration process. Figure 2 illustrates this process being performed on NOAA AR 10486, which was a delta-class sunspot group.

The image is first strongly smoothed and the zero Gauss contours identified. Smoothing effectively removes the small-scale structures that generate extraneous inversion lines away from the PIL. A vector field is then calculated using an $\alpha=0$ linear force-free field model (Alissandrakis 1981; Falconer et al. 2002). The first stage ends by identifying continuous zero Gauss contours with a horizontal field gradient on both sides above a specified threshold, and with a strong model vector magnetic field strength. This process is repeated for a less smoothed image. The continuous segments of this stage are superimposed on the result of the previous stage (Fig. 2 left) and used as the output contour wherever the two iterations

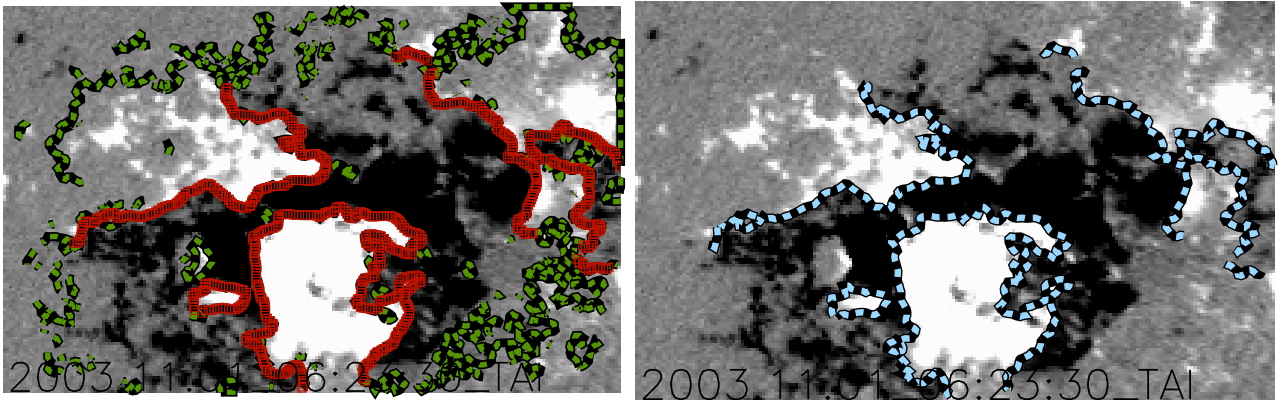


Fig. 2.— Left – An image of NOAA AR 10486 overlaid with the results from the primary inversion line (PIL) algorithm overlaid. The inversion line output from a less smoothed image (green dashes) and a more smoothed image (red squares) are superimposed. The program selects inversion line segments where the two overlap. Right – The agreement between the green dashes and red squares yields the dashed blue line: the nearest approximation to the PIL in this iteration.

agree within a specified number of pixels. Finally, this method is applied to compare the results from a completely unsmoothed image and the results from the previous stage. This procedure emphasizes the connectivity of the line segments, inversion line stability over time, and it reduces noisy extensions of the PIL. Inspection of the segment shows that the algorithm produces a fairly accurate representation of the PIL (see Fig. 2 right). It is difficult to define a singular PIL in ARs with exceedingly complex geometries, such as delta sunspots (e.g. NOAA AR 10486). In these cases, our algorithm identifies multiple PILs that are a fair match to those that have been subjectively determined.

Conceptually, a longer PIL indicates a more complex magnetic field structure. Furthermore, a large gradient near the inversion line indicates an appreciable difference in the magnetic field over a relatively small distance. This is indicative of shearing or twisting of the magnetic fields. Therefore, we calculate the length, which is a simple sum of the line segments, and the field gradient across the primary inversion line.

2.2.3. *Effective Separation*

The effective separation was first investigated by Chumak and Chumak (1987). Chumak et al. (2004) and Guo (2006) found the effective distance between the two bipolar regions of an AR to be a useful parameter for flare prediction. First, the two polarities are weighted

by the amount of flux they contain and the centers are found. The distance between the flux weighted centers is indicative of how separated the bipoles are (Guo and Zhang 2006). A small effective separation is indicative of a compact AR. Such regions are likely to contain a lot of intermingled flux, which may lead to large gradients.

Active regions consisting of more complex geometries than a bipolar distribution may produce separations that are difficult to interpret with this type of measure. No modification is applied to the method of calculation for such ARs, which should be considered when weighing the results yielded from this measure. Georgoulis and Rust (2007) proposed a similar measure, B_{eff} , which effectively describes the amount of magnetic connection within an AR by comparing the net flux to the distance between magnetic footpoints, as determined by the magnetic charge topology model (Barnes et al. 2005). They found a greater than 95% probability of M- or X-class flaring for ARs with critically high values of B_{eff} .

2.2.4. Gradient-Weighted Inversion-Line Length (GWILL)

GWILL corresponds closely to the parameter L_{SG} proposed by Falconer et al. (2003). This parameter is calculated by applying the equation

$$GWILL = \sum \nabla B_{\perp} \quad (1)$$

where the sum runs along the entire length of the PIL, and ∇B_{\perp} is calculated across the PIL. This measure tends to emphasize regions of the AR that are strongly sheared and magnetically complex.

Schrijver (2007) created a similar parameter, R , that was a measure of the unsigned flux near such high-gradient, strong-field polarity-separation lines. He found a strong correlation between an AR’s propensity to flare and the value of $\log R$. Falconer et al. (2003) proposed using the length of the segment of the PIL with a longitudinal field gradient above 50G per megameter, L_{SG} , as a measure correlated to CME initiation. L_{SG} is a proxy for the strong shear length, L_{SS} , which can only be derived from vector magnetograms. L_{SG} uses model transverse fields (as GWILL does) in place of the observed vector field used for L_{SS} . Whereas Falconer et al. (2003) cut off the length of the PIL with the gradient below a threshold, this study simply weights all segments by the gradient. The resultant quantity should be a better predictor of flaring than the standard PIL because GWILL benefits from the best of both the PIL and the gradient across it. GWILL is larger for ARs that have long PILs, which are indicative of a complex field structure, and is also larger when there are high gradients, which is indicative of shearing. Another primary difference from Falconer (2003) is that this study is searching for a correlation with flares instead of CMEs, and thus

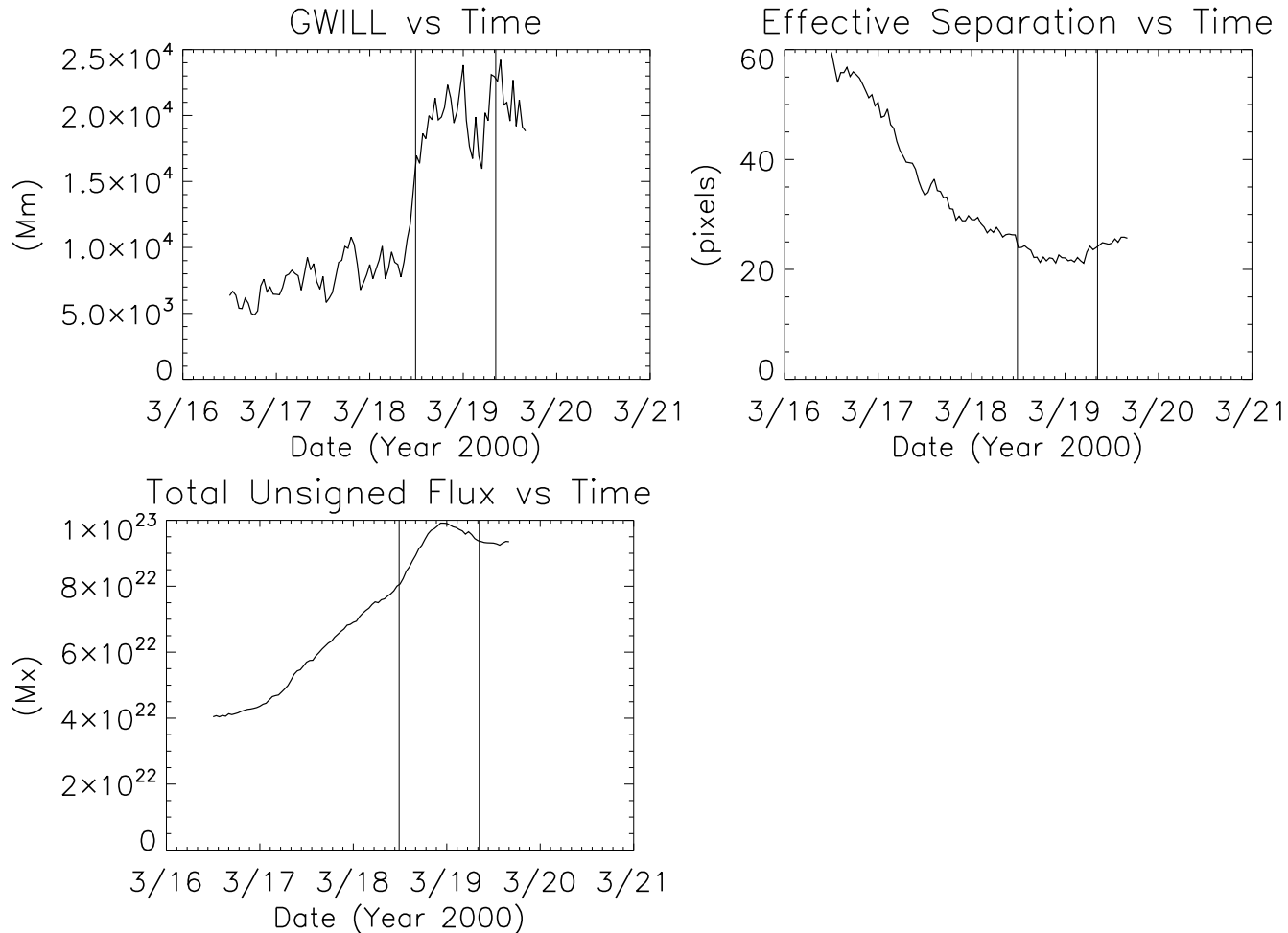


Fig. 3.— The evolution of the gradient-weighted inversion-line length (GWILL) (top-left), effective separation (top-right), and total unsigned flux (bottom-left) during the disk passage of AR 8910. Units are in megameters, pixels, and Maxwells, respectively. Vertical lines indicate the temporal locations of M or X class flares. Note the clear increase (decrease) in GWILL and flux (effective separation). This is a representative, but not necessarily universal, response to flares.

a direct comparison is difficult.

2.3. Program Outputs

In order to determine a relationship between these indices and the ARs energetic event productivity, we use the online GOES solar x-ray flare catalog available from the National

Geophysical Data Center. Each flare has been associated with an AR through their observed locations in $H\alpha$ images. Flares not associated with any specific AR were not included in our analysis. For each AR, a time series was created for each calculated variable. Figure 3 shows an example with the temporal location of any M or X class flares indicated.

For each AR, the parameters for every magnetogram included in this study were placed in a single table that is available online². There are 71,324 magnetograms listed in our Great Table. For each NOAA AR the table lists the set of relevant magnetograms, including the NOAA AR number, date, time, MDI FITS file identifier, Carrington location, pixel coordinates of the sub-image, and the five calculated parameters. Another table listing the date, start time, end time, time of maximum flux, solar location, GOES classification, and the associated NOAA AR number of each of the 12,576 flares is also available².

3. Data Analysis and Results

The parameters calculated for each of the 1,075 ARs are used to search for a relationship to solar flares. Superposed Epoch (SPE) plots provide a sensitive tool to discover the average response of a complex, variable system to a certain type of event at a particular set of times (e.g. Chree 1913; Singh and Badruddin 2006). Essentially, the SPE plots produced in this study are the combination of multiple individual time series with the temporal location of a selected set of flares aligned. One can align to any set of keytimes. The analysis code accepts a list of keytimes, or a keylist, and gathers the available data from the Great Table. For any specific nonpotentiality measure, the time series are aligned relative to the keytimes to compute the average response to the event (see Figs. 4-6). Since MDI takes magnetograms at a 96-minute cadence, our data series exist as a succession of points 96 minutes apart. Separate keylists were constructed for the X-class, M-class, and B-C- class (quiet) flares. The observation of any M- or X-class flares in an AR was cause to exclude that AR from being included in the quiet keylist. This reduces the size of the quiet keylist, but avoids the problem that larger flares tend to overshadow the effects of the smaller ones.

In addition, a control set was created that includes the ARs associated with no flaring at all during the ARs passage within 30 degrees of disk center (Dead Silent regions). Since an AR could flare while on the far side of the sun, we chose to enforce the 30 degree limitation on the Dead Silent definition to keep the analysis consistent with the 30 degree limitation placed on the selection of MDI data (see Section 2.1). For Dead Silent regions, a random instant in the time series was chosen to act as the keytime to eliminate any location-based

²<http://soi.stanford.edu/data/tables>

bias. However, we required that at least three data points be available before and after this random instant (e.g. if the random instant chosen was the first observation within the 30 degree limit, no prior data would be available and a new random instant must be selected).

If a flaring AR contained more than one flare, we included it multiple times and aligned the time series so that each flare would be at $t=0$. In the forecasting community, it is a rule of thumb that an AR that has flared recently is likely to flare again – this is known as flare persistence (Sawyer 1986). At times of particularly frequent flaring, the magnetic fields may not have time to fully relax after a flare before another occurs. This means that the signal

Normalized Mean and Standard Deviation of GWILL

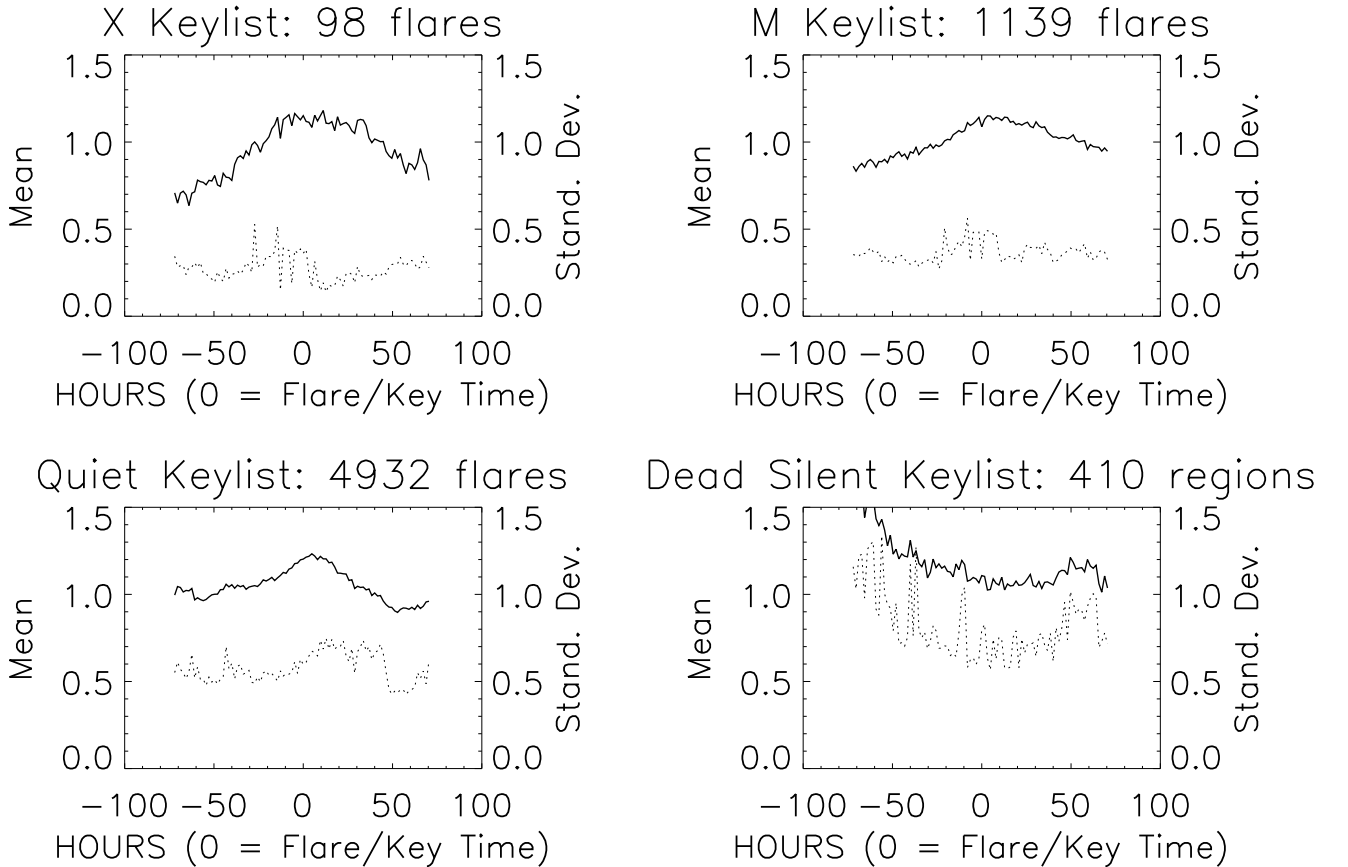


Fig. 4.— Superposed epoch (SPE) plots of GWILL for X-class flares, M-class flares, B- and C-class flares (quiet), and regions lacking any flares (Dead Silent). Flares occurred within 96 minutes after the zero time. The solid and dashed lines represent the normalized mean and normalized standard deviation, respectively.

for any such flare may be obscured. The analysis considered every flare for an AR instead of choosing a single flare with a predetermined condition. The goal was to improve statistics and detect any weak systematic signal with SPE analysis. The total number of flares in each keylist was 98, 1139, and 4932 for the X, M, and quiet keylists, respectively. The total number of ARs lacking any flares was 410, which constituted the Dead Silent keylist.

The first four statistical moments of each time in the SPE were calculated. Our primary focus was on the mean and standard deviation. Our goal was to see what tends to happen at each point in time relative to the flare time, thus we are primarily concerned with the fractional change. Therefore, data shown in Figures 4 to 6 have been normalized by dividing the time series for each keytime by the median value computed for that interval before combining them. We chose to normalize by the median, as opposed to the mean, in order to generate a normalization less sensitive to outliers. We included the Dead Silent regions as a control, as we did not expect that a flaring AR would behave the same as a non-flaring AR. The results confirm this expectation and suggest that the signal is truly a response to the flares.

Figure 4 shows a clear trend in GWILL – a gradual apex centered approximately on the flare time ($t=0$) whose magnitude is greater for X-class flares. The control test (lower right panel) shows that GWILL for ARs lacking any flaring tends to decrease during disk passage. This decrease may be partially due to a selection bias – regions that are growing are increasing in complexity and are therefore more likely to flare, thus excluding them from the Dead Silent keylist. This suggests that on average, an AR’s PIL and the gradient across it will decrease when an AR is not producing flares. In Figure 4, note the strong disparity between ARs with flaring and those without. The size of the peak is appreciably larger for X-class flares. Table 1 summarizes the percent changes from -40 and -20 hours to the keytime for each quantity.

Table 1: Percent Changes in Parameter Between Flare Time and 40/20 Hours Prior

	GWILL		Eff. Sep.		Total Flux	
	-40 hr	-20 hr	-40 hr	-20 hr	-40 hr	-20 hr
X	35.3	18.2	-25.3	-19.0	21.0	8.9
M	16.3	10.4	-13.4	-8.8	12.1	6.6
C + B (quiet)	17.3	10.1	-16.8	-8.1	15.7	7.8
Dead Silent	16.5	-3.2	-0.16	0.28	2.1	1.5

The effective separation (Fig. 5) shows a similar flare dependency to GWILL, however, the general trend is now inverted. The separation definitely decreases prior to flaring and

Normalized Mean and Standard Deviation of Effective Separation

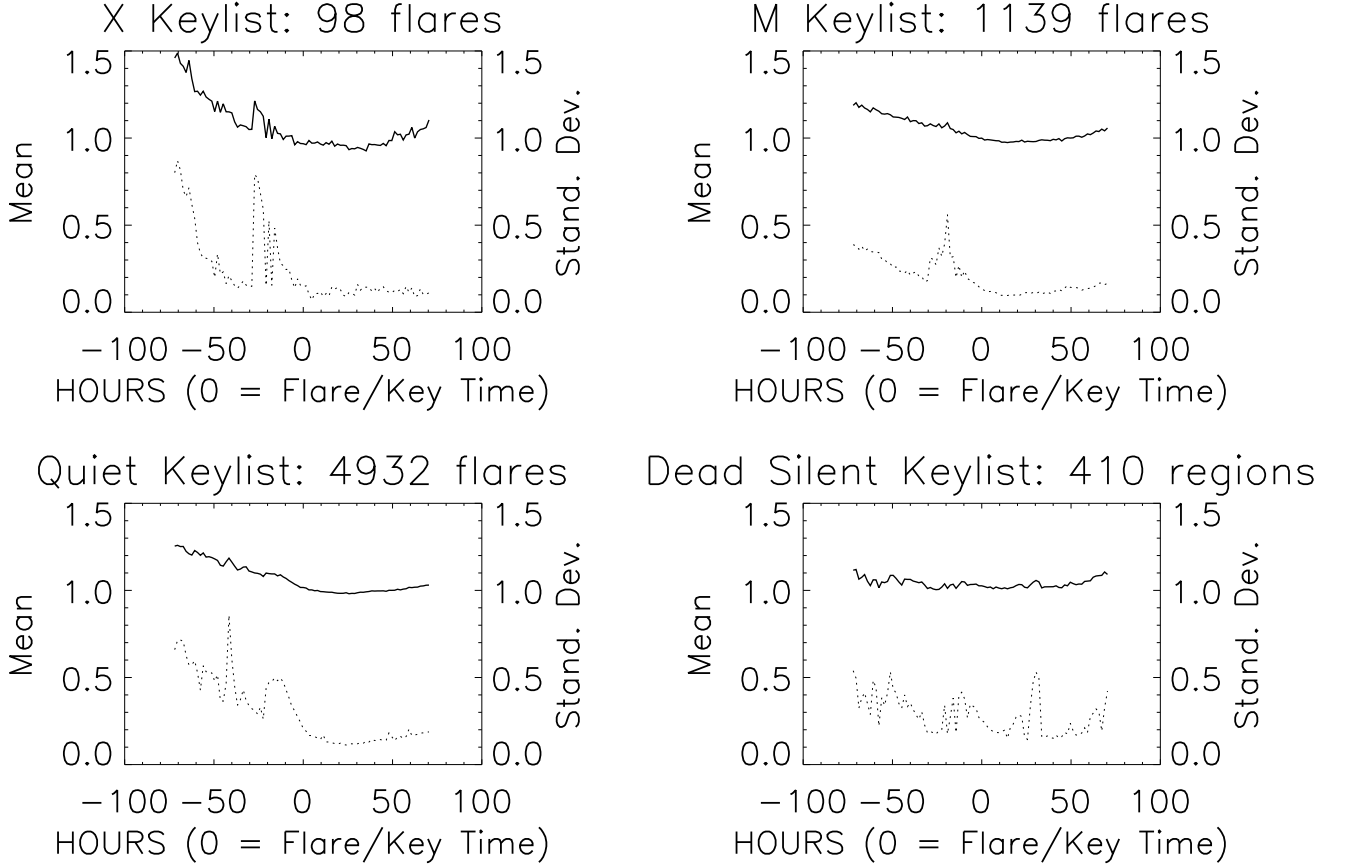


Fig. 5.— The same as Figure 4, but for the effective separation. Again, note the difference between ARs associated with flares and those that are not. The effective separation remains roughly constant if no flaring occurs, whereas it tends to reach a minimum value near the time of flaring if flaring does occur. A steady decrease prior to flaring is followed by a very gentle recovery period. The size of this response is appreciably larger for X-class flares.

increases very slightly after. The control test (lower right panel) confirms that the separation between bipolar regions remains nearly constant in ARs that do not produce flares.

Finally, the total unsigned flux (Fig. 6) demonstrates very similar behavior to GWILL. The primary difference is that the control test (lower right panel) produced a nearly constant value of total flux. Also, the percent changes for total unsigned flux were markedly smaller than GWILL. Again, X-class flares generate a stronger response than weaker flares. We do not include separate plots for the PIL and the gradient across it because GWILL includes

Normalized Mean and Standard Deviation of Total Unsigned Flux

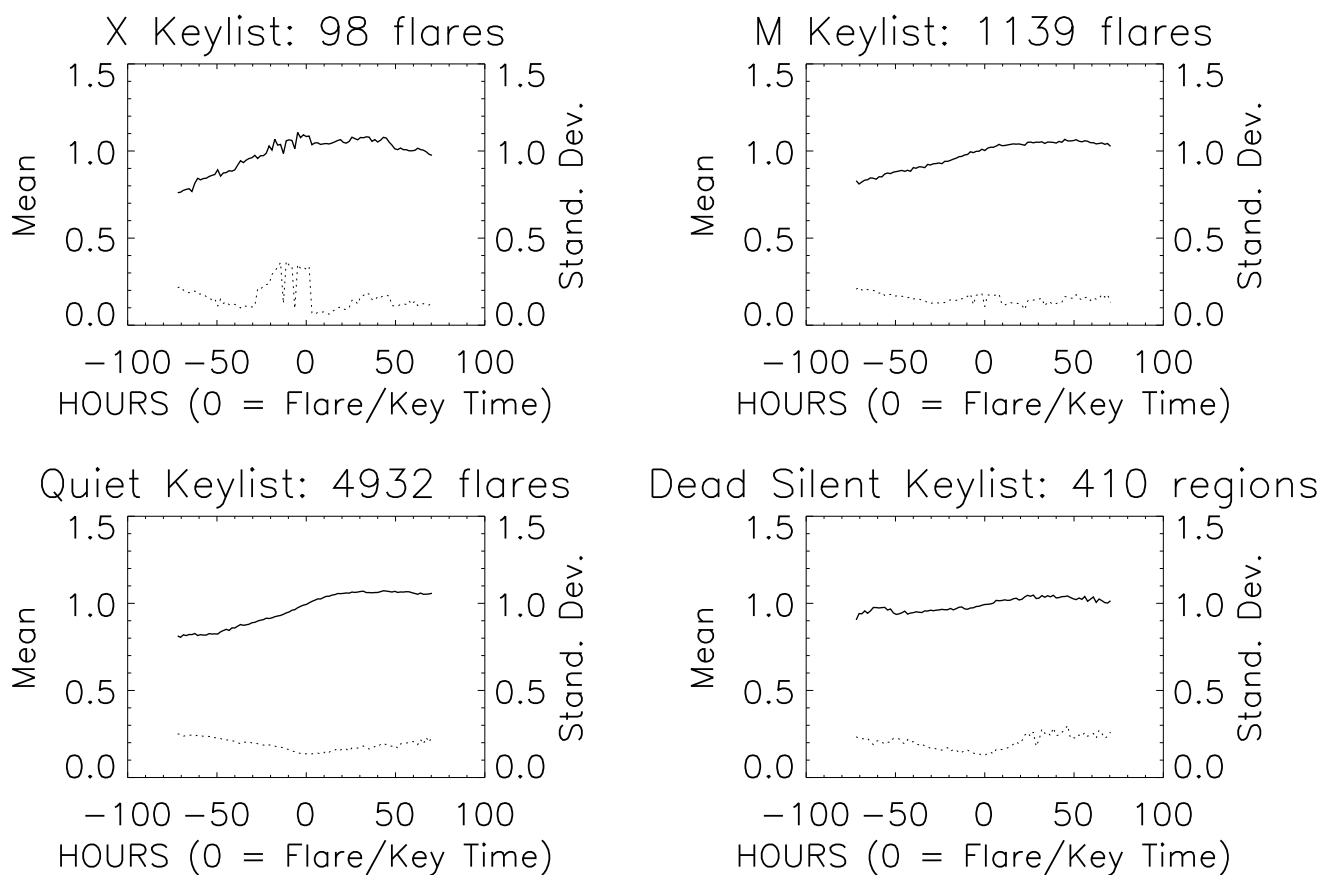


Fig. 6.— The same as Figures 4 and 5, but for the total unsigned flux. It is more difficult to distinguish flare-associated from flare-unassociated ARs using this parameter. On average, ARs tend to increase in total unsigned flux during disk passage. If a flare occurs, this increase tends to be larger. Again, the response is much stronger for X-class flares.

the most responsive parts of both.

The standard deviation for the Dead Silent keylist for these three measures is worth noting. In GWILL (Fig. 4 lower-right), the standard deviation is relatively large indicating a lack of signal, as expected. However, standard deviation is not as large in effective separation and total flux (Fig. 5 and Fig 6. lower-right). This difference is likely due to GWILL values that are closer to its fundamental noise level. When values of the parameter are sufficiently low, the standard deviation becomes noticeably larger.

Close inspection of Table 1 will reveal that the percent changes found for the M and quiet keylists are very similar. The quiet keylist often has values that are slightly larger than the M keylist. This may be due to the greater number of C and B flares compared to M flares. This result suggests that given greater numbers, SPE analysis is sensitive enough to detect a signal, even when the presumed cause of the signal is significantly weaker.

3.1. Forecasting and Prediction

The results of our SPE analysis are the detection of a signal that is small in comparison to the typical time variations of any individual AR. As the total number of contributing data series to a single SPE plot decreases, the standard deviation increases and becomes more erratic. For an individual AR, complex physical processes tend to mask the signal of any single measurable parameter in noise. Only with a large sampling of data is it possible to use the power of statistics to enhance the strength of this signal.

Given the values in Table 1, one might propose to reverse the situation: search for a percent change above a specific threshold in an AR and expect to see a flare of a particular intensity. Barnes & Leka (2008) performed a skill score analysis to quantify the predictive ability of several photospheric magnetic field parameters. They found that the performance of these parameters is only slightly better than uniform or climatological forecasts. We performed a similar analysis and determined, as expected, that it is not possible to obtain good predictive results.

As an example, Table 2 shows the results for the largest percent change value we identified, a 35% increase in GWILL in the 40 hours prior to the time of flaring. For each AR, a prediction is made every 96 minutes in the time series based on the percent change in the preceding 40 hours. If the percent change was above 35%, an X-class flare was predicted. Conversely, an “X-class all-clear” prediction was made if the percent change was below 20%. In the intermediate case, from 20-35%, no prediction was made. We then compared the predictions to the observations from GOES. We required that the flare occur within 6 hours of

the time it was predicted in order to consider it a true-positive result. False-positive results indicate that an X-class flare was predicted, but there was none within the 6-hour limit. If a flare occurred when the all-clear was predicted, it was labeled a false negative and if no flare occurred with none predicted, it was labeled a true negative. In addition to the 6-hour limit, we experimented with acceptable flare windows of 3 and 9 hours and found that the results were not significantly altered. This is likely due to the fact that X-class flares are rare events so changing the flare window by a few hours is not likely to influence the number of detected flares.

Using this contingency table (Tbl. 2), the Gilbert (GS) and Heidke (HSS) skill scores were calculated using the equations specified by the Space Weather Prediction Center [SWPC 2007]. We found that $GS = 0.0077$ and $HSS = 0.6944$. The primary difference between these two skill scores is that only HSS takes the true negative results into account. True negative results have a large impact on the value of the skill score because they dominate our contingency table. Another more subtle difference between GS and HSS is in their methods for correcting chance forecasts. GS factors in the number of true positives due to chance, whereas HSS corrects all random forecasts (i.e. true positives and true negatives due to chance). The value obtained for GS suggests that even GWILL, the parameter most highly associated with flaring, is a poor real-time predictor of flares. As HSS has possible values ranging from -1 to 1, the value of HSS obtained here suggests that GWILL is capable of predicting the all-clear with more success than random forecasts. However, the ability to predict when an X-class flare will occur is our primary interest since it requires some understanding of the mechanisms associated with flare production. While it has been shown that a predictive understanding is not yet possible, this does not nullify the primary result establishing a statistical correlation between solar flare occurrence and the photospheric magnetic field configuration.

Table 2: Contingency Table: Results of predicting an X-class flare based on at least a 35% change in GWILL at each 96 minute step in the time series.

	True	False
Positive	87	11,215
Negative	25,517	54

4. Conclusions

Superposed epoch analysis has the ability to pick out weak systematic responses. While many of the commonly studied very large ARs have been found to have a degree of high-energy-event predictability, it is important to study what happens to a typical active region in the time surrounding such events. In this study, a change in three primary parameters was discovered to be well correlated with the presence of flares. X-class flares are correlated with a stronger response in these parameters. However, the changes are too small to be predictive in an individual case-by-case sense. This is consistent with the findings of Leka and Barnes (2003b), who are skeptical of the possibility of using only line-of-sight magnetic data to predict CMEs or flares. Leka and Barnes (2006) found that the magnetic field at the photosphere is only moderately related to the flare productivity of the region. Barnes and Leka (2008) show that the best measures of magnetic nonpotentiality are as good at forecasting flares as independent methods, and suggest that forecasting may be improved by combining these methods. We concur with these conclusions and urge the forecasting community to carefully consider any prediction results based on longitudinal magnetograms.

In the course of this study, algorithms were developed for the automatic collection and extraction of AR patches from MDI magnetograms, as well as the automatic calculation of variables on all these data. The programs and our results from them have been made available online. However, access to the MDI database is required and editing of the IDL code may be necessary. Development of these routines is underway for use on the Solar Dynamics Observatory’s Helioseismic Magnetic Imager (SDO/HMI) data.

We have also begun preliminary research into the change in total flux over an AR’s disk passage. Many researchers have found that rapid changes in flux are well correlated with an ARs propensity to flare (e.g. Wang et al. 1994, Choudhary et al. 1998). We hope to conduct a study similar to the present investigation to analyze this quantity statistically. Petrie and Sudol (2010) have shown that local small-scale changes within the AR are associated with flaring. This suggests that some information may be lost when parameterizing an AR image with a single number. Future statistical studies should consider including this type of spatial analysis. Many of the most promising flare-predictive magnetic parameters require the use of vector data, which are not currently available in a long duration, frequent cadence form. With the recent launch of SDO and continuing operation of SOLIS, such a database will be available to perform an analysis that could parallel the present paper. HMI produces 4096^2 pixel full-disk vector magnetograms as rapidly as every 90 seconds. In addition to allowing for a more detailed study of the photospheric magnetic field in space and time, this will open access to the transverse components where much of the enigmatic relationship to solar flares is likely to be found.

This work was supported by NASA MDI Grant NNX09AI90G. SOHO is a project of international cooperation between ESA and NASA. The authors would like to thank the reviewer for insightful and helpful comments.

REFERENCES

- Alissandrakis, C. E., 1981, *Astron. Astrophys.*, 100, 197
- Barnes, G., Longcope, D. W., & Leka, K. D. 2005, *ApJ*, 629, 561
- Barnes, G., Leka, K. D. 2006, *ApJ*, 646, 1303
- Barnes, G., & Leka, K. D. 2008, *ApJ*, 688, L107
- Bokenkamp, N. 2007, Senior Thesis, Stanford University
- Choudhary, D. P., & Ambastha, A. 1998, *Sol. Phys.*, 179, 133
- Chree, C. 1913, *Philosophical Transactions Royal Society London Series*, 212, 75
- Chumak, O. V., & Chumak, N. V. 1987, *Kinematika i Fizika Nebesnykh Tel*, 3, 7
- Chumak, O., Zhang, H., & Gou, J. 2004, *Astronomical and Astrophysical Transactions*, 23, 525
- Falconer, D. A., Moore, R. L., & Gary, G. A. 2002, *ApJ*, 569, 1016
- Falconer, D. A., Moore, R. L., & Gary, G. A. 2003, *J. Geophys. Res.*, 108, 1380
- Falconer, D. A., Moore, R. L., & Gary, G. A. 2008, *ApJ*, 689, 1433
- Freeland, S. L., & Handy, B. N. 1998, *Sol. Phys.*, 182, 497
- Georgoulis, M. K., & Rust, D. M. 2007, *ApJ*, 661, L109
- Guo, J. & Zhang, H. 2006, *Sol. Phys.*, 237, 25
- Krall, K. R., Smith, J. B., Hagyard, M. J., West, E. A., & Cummings, N. P. 1982, *Sol. Phys.*, 79, 59
- Leka, K. D., & Barnes, G. 2003a, *ApJ*, 595, 1277
- Leka, K. D., & Barnes, G. 2003b, *ApJ*, 595, 1296

- Leka, K. D., & Barnes, G. 2007, *ApJ*, 656, 1173
- Liu, Y., Norton, A. A., & Scherrer, P. H. 2007, *Sol. Phys.*, 241, 185
- Metcalf, T. R., Litao, J., McClymont, A. N., Canfield, R. C., & Uitenbroek, H. 1995, *ApJ*, 439, 474
- National Research Council (NRC). 2008, *Severe Space Weather Events*, National Academies Press
- Petrie, G.J.D., & Sudol, J. J. 2010, *ApJ*, in preparation
- Sawyer, C., Warwick, J. W., & Dennett, J. T. 1986, *Solar Flare Prediction*, Boulder: Colorado Associated University Press
- Scherrer, P. H., et al. 1995, *Sol. Phys.*, 162, 129
- Schrijver, C. J. 2007, *ApJ*, 655, L117
- Schrijver, C. J. 2008, *Advances in Space Research*, 43, 803
- Silva, A. V. R., et al. 1996, *ApJ*, 106, 621
- Singh, Y. P., & Badruddin. 2006, *J. Atm. Solar-Terr. Phys.*, 68, 803
- Space Weather Prediction Center. 2007, *Forecast Verification Glossary*, Boulder, CO: NOAA, http://www.swpc.noaa.gov/forecast_verification/Glossary.html
- Tanaka, K., & Nakagawa, Y. 1973, *Sol. Phys.*, 33, 187
- Wang, T., Xu, A., & Zhang, H. 1994, *Sol. Phys.*, 155, 99